

Nonthermal antiferromagnetic order and nonequilibrium criticality in the Hubbard model

Naoto Tsuji,¹ Martin Eckstein,² and Philipp Werner¹

¹*Department of Physics, University of Fribourg, 1700 Fribourg, Switzerland*

²*Max Planck Research Department for Structural Dynamics,
University of Hamburg-CFEL, 22607 Hamburg, Germany*

(Dated: June 2, 2021)

We study dynamical phase transitions from antiferromagnetic to paramagnetic states driven by an interaction quench in the fermionic Hubbard model using the nonequilibrium dynamical mean-field theory. We identify two dynamical transition points where the relaxation behavior qualitatively changes: one corresponds to the thermal phase transition at which the order parameter decays critically slowly in a power law $\propto t^{-1/2}$, and the other is connected to the existence of nonthermal antiferromagnetic order in systems with effective temperature above the thermal critical temperature. The frequency of the amplitude mode extrapolates to zero as one approaches the nonthermal (quasi)critical point, and thermalization is significantly delayed by the trapping in the nonthermal state. A slow relaxation of the nonthermal order is followed by a faster thermalization process.

PACS numbers: 71.10.Fd, 64.60.Ht

In many physical systems out of equilibrium, phase transitions occur as a real-time process of symmetry breaking or symmetry recovery. Examples for such “dynamical phase transitions” include the evolution of the Universe [1], liquid helium [2], and photoinduced phase transition in solids [3–5]. The macroscopic aspects are often described by the time-dependent Ginzburg-Landau theory, where the order parameter is supposed to vary sufficiently slowly in time and space, so that the system can be considered to be locally close to thermal equilibrium. On the other hand, recent experimental developments of time-resolved measurement techniques in solids [6] and cold atoms [7] allow one to study dynamical phase transitions very far from equilibrium on the microscopic time scale of correlated quantum systems. In these cases, a “near-equilibrium” description might not be applicable. For instance, it has been recently suggested that superconductivity can be induced above the equilibrium critical temperature (T_c) by coherently exciting certain lattice vibrations, and that it lasts for a relatively long time (a few tens of ps) before thermalization occurs [5]. This observation is reminiscent of the prethermalization phenomenon [8–11], or the dynamics in the presence of a nonthermal fixed point in relativistic quantum field theories [12]. A fundamental question that we pose here is if the existence of such a nonthermal fixed point in correlated condensed matter systems allows symmetry broken states to survive above T_c , and how it affects the dynamics.

An important and still unresolved issue is how to characterize a nonequilibrium phase transition and its critical behavior for quantum systems [13, 14]. Previous studies have in particular focused on the dynamics near quantum phase transitions in low dimensional systems (e. g., Refs. [15–18]). Higher dimensional systems are usually expected to show a thermal criticality out of equilibrium since quantum fluctuations are well suppressed. In this Letter, we study a dynamical phase transition for a simple microscopic model of correlated materials, namely the Hubbard model. In equilibrium, the model exhibits a phase transition from paramagnetic (PM) to antiferromagnetic (AFM) order [see the phase diagram in

Fig. 1(a)]. By changing the interaction in time, we cross the phase boundary dynamically. In particular, we explore the weak-coupling regime of the Hubbard model (for the strong-coupling side, see our complementary work [20]). Contrary to the naive expectation, we find that the nonequilibrium relaxation behavior can be very different from the thermal one even in the large-dimensional limit. A new phenomenon that we demonstrate here is that in addition to the thermal critical point there exists one more quasicritical point (or sharp crossover) at which some time (energy) scale almost diverges (vanishes). Between these points, the system is trapped in a nonthermal “ordered” state [Fig. 1(b)], where the order parameter stays nonzero even though the effective temperature (which will be defined below) is above T_c .

The model Hamiltonian is given by

$$H(t) = \sum_{k\sigma} \epsilon_k c_{k\sigma}^\dagger c_{k\sigma} + U(t) \sum_i \left(\hat{n}_{i\uparrow} - \frac{1}{2} \right) \left(\hat{n}_{i\downarrow} - \frac{1}{2} \right),$$

where ϵ_k is the band dispersion, $c_{k\sigma}^\dagger$ ($c_{k\sigma}$) is a creation (annihilation) operator of fermions with spin σ , U is the (time-dependent) interaction strength, and $\hat{n}_{i\sigma} = c_{i\sigma}^\dagger c_{i\sigma}$. For convenience, we take a semicircular density of states, $D(\epsilon) = \sqrt{4 - (\epsilon/t^*)^2}/(2\pi t^*)$, and use t^* (t^{*-1}) as the unit of energy (time). We only show results for the half-filling case. The initial state is in thermal equilibrium with temperature T , which is chosen such that the initial value of the staggered magnetization $m = \langle |\hat{n}_\uparrow - \hat{n}_\downarrow| \rangle$ is 0.4. The interaction is changed as $U(t) = U_i + (U_f - U_i)t/t_q$ ($0 \leq t \leq t_q$) with quench time $t_q = 8$ fixed. The interaction quench can be implemented in cold atom systems with the use of the Feshbach resonance, or by modifying the depth of the lattice potential, and has also been proposed to be possible in solids driven by strong electric fields [21, 22].

The time evolution of the Hubbard model with AFM order is studied with the nonequilibrium dynamical mean-field theory (DMFT) [23, 24]. It becomes exact in the large dimensional limit [25], where the self-energy becomes local in space but keeps dynamical correlations. When one allows for AFM

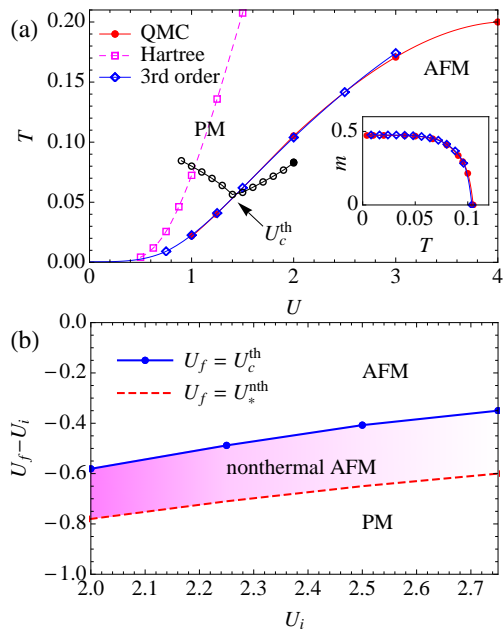


FIG. 1: (color online). (a) Equilibrium phase diagram of the Hubbard model in the weak-coupling regime at half filling, calculated by DMFT with several different impurity solvers. QMC data are taken from Ref. 19. Effective temperatures for quenches from a fixed initial state ($U_i = 2$, black dot) to various final states (open dots) are shown. Inset: Staggered magnetization m as a function of T at $U = 2$. (b) Nonequilibrium phase diagram for a quench $U_i \rightarrow U_f$ with the fixed initial magnetization, $m(0) = 0.4$. For $U_f > (<)U_c^{\text{th}}$, the system finally thermalizes to an AFM (PM) state. A nonthermal AFM order emerges in the colored region. The shading indicates the increasing lifetime of the nonthermal AFM state as U_i is reduced.

states in the single-site DMFT, the self-consistency condition reads $\Lambda_\sigma(t, t') = t^{*2}G_\sigma(t, t')$ [20, 23] [$\Lambda_\sigma(t, t')$: hybridization function]. Since we are interested in the microscopic dynamics in a single magnetic domain, the system is assumed to take a spatially homogeneous configuration.

In order to treat the long-time behavior of symmetry broken states, we adopt the third-order weak-coupling expansion as an impurity solver, i.e., expand all the self-energy diagrams, including the Hartree term, by Weiss Green functions $G_{0\sigma}(t, t')$ (bare propagators) up to third order in U . Although the bare expansion is not a conserving approximation in the sense of Baym and Kadanoff, it turns out to work remarkably well in the weak-coupling regime ($U \lesssim 3$). For instance, the total energy is approximately conserved with negligibly small drifts. By comparison to quantum Monte Carlo (QMC) results [19], we confirmed that T_c and m in equilibrium are correctly reproduced [Fig. 1(a)], which is a considerable improvement from the Hartree approximation [Fig. 1(a)] and the second-order iterative perturbation theory [23].

Let us first look at results for quenches from $U_i = 2$ to various $U_f (< U_i)$. As shown in Fig. 2(a), $m(t)$ quickly decreases after the quench due to the reduction of U , and starts to oscillate coherently (amplitude mode) with a slow drift. As U_f

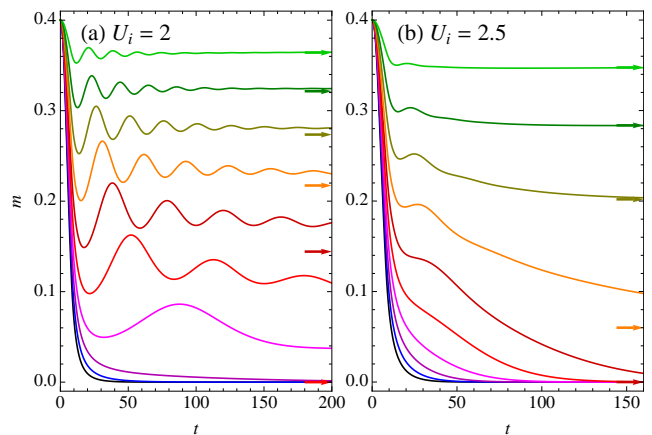


FIG. 2: (color online). Time evolution of m for quenches (a) $U_i = 2 \rightarrow U_f = 1.0, 1.1, \dots, 1.9$ (from bottom to top), and (b) $U_i = 2.5 \rightarrow U_f = 1.5, 1.6, \dots, 2.4$. The arrows indicate the corresponding thermal values m_{th} reached in the long-time limit.

decreases below ~ 1.2 , the oscillation disappears, and m exponentially decays to zero. Assuming that the nonintegrable Hubbard model thermalizes, the long-time limit of the order parameter is determined by the thermal value m_{th} at some effective temperature T_{eff} . Since the total energy is conserved after the quench ($t \geq t_q$) in the isolated system, T_{eff} is given by the temperature of the equilibrium system with the same total energy. The final thermalized states are plotted as open dots in Fig. 1(a). Since we are considering rather slow changes ($t_q = 8$) of U , the final states roughly keep track of the constant entropy curve [26].

The evaluated m_{th} are indicated by arrows in Fig. 2, and are plotted as a function of U_f in Fig. 4. One notices that the center of the oscillation of m deviates more and more from m_{th} as U_f is reduced. Surprisingly, at $U_f = U_c^{\text{th}} = 1.42$, where m_{th} vanishes $\propto |U_f - U_c^{\text{th}}|^\beta$ (Fig. 4) with the mean-field exponent $\beta = \frac{1}{2}$ (thermal phase transition), m still exhibits oscillations around a nonzero value for a long time. This suggests that the system is effectively trapped in a nonequilibrium quasisteady state, or close to a nonthermal fixed point, which allows for a long-lived symmetry broken state with T_{eff} above T_c . In the paramagnetic phase, the system shows prethermalization [9–11]; i.e., the momentum-integrated quantities such as the double occupancy thermalize faster than momentum-dependent quantities (e. g., the momentum distribution). Here a new observation is that the order parameter m , even though it is momentum integrated, also stays nonthermal, allowing the symmetry-broken state to survive for a long time. This can be attributed to the presence of “classical fluctuations” [12] in the Hartree term, which is absent in the paramagnetic phase.

To look at the qualitative change of the relaxation behavior around $U_f \sim 1.2$ more closely, we calculate the momentum distribution $n_k(t) \equiv \langle c_{k\sigma}^\dagger(t)c_{k\sigma}(t) \rangle$ [27]. In Fig. 3, one can clearly see the qualitative difference of n_k between (a) $U_f = 1.4$ and (b) $U_f = 1.2$. In the former case, waves are

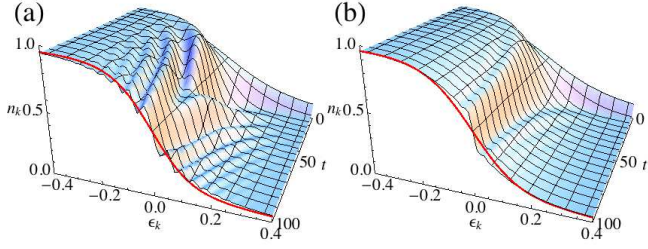


FIG. 3: (color online). Time evolution of the momentum distribution n_k for quenches $U_i = 2 \rightarrow$ (a) $U_f = 1.4$ and (b) $U_f = 1.2$. The curves at $t = 100$ are thermal distributions achieved in the long-time limit.

continuously generated at high energy, and cascade down to the lower energy region. They eventually reach the Fermi energy $\epsilon_k = 0$, and lead to an oscillation of the slope $\partial_\epsilon n$ at $\epsilon_k = 0$ [27]. In the latter case, the wave fronts never arrive at the Fermi energy but accumulate near $\epsilon_k = 0$, which results in a steepening slope $\partial_\epsilon n$. This evolution is opposite to a heating effect, where an initially sharp momentum distribution is smeared out. Since the n_k in Fig. 3(b) is very different from a thermal distribution [curve at $t = 100$ in Fig. 3(b)] the fast relaxation of m for $U_f \leq 1.2$ [Fig. 2(a)] is due to dephasing, not thermalization.

To characterize the nonthermal transition observed around $U \sim 1.2$ quantitatively, we evaluate the relaxation time τ_{deph} for the dephasing of $m(t)$ by fitting with $e^{-t/\tau_{\text{deph}}}$. As shown in Fig. 4(a), the dephasing critically slows down as $\tau_{\text{deph}} \propto |U_f - U_*^{\text{nth}}|^{-1}$ with $U_*^{\text{nth}} = 1.23$ (nonthermal transition point). At $U_f = U_*^{\text{nth}}$, $m(t)$ shows a power-law decay of $t^{-1/2}$ until thermalization starts to take place around $t \sim 100$. This indicates that one more quasicritical point with an associated diverging time scale exists away from the thermal critical point ($U_f = U_c^{\text{th}}$). Moreover, a sharp kink is observed at $U_f = U_*^{\text{nth}}$ in the plot of the inverse of the steepest slope $(\partial_\epsilon n)^{-1} = (\max_t \{|\partial_\epsilon n(t)|\})^{-1}$ at $\epsilon_k = 0$ [Fig. 4(a)]. Because a true discontinuity in the momentum distribution function, with $(\partial_\epsilon n)^{-1} = 0$, would correspond to a power-law decay of the density correlations in space, one may thus note that at the nonthermal critical point the system evolves through an almost “critical state” before thermalization sets in. We also determined the frequency ω_m of the amplitude mode of m and the frequency $\omega_{\partial_\epsilon n}$ of the oscillation of $\partial_\epsilon n$ at $\epsilon_k = 0$ for $U_f > U_*^{\text{nth}}$ by measuring the peak-to-dip distance of the oscillations. Note that near the critical point the period of the oscillation exceeds the lifetime (~ 100) of the trapped state, so that a meaningful measurement is not possible. However, the results in Fig. 4(a) indicate that ω_m and $\omega_{\partial_\epsilon n}$ extrapolate to zero as $\sim |U_f - U_*^{\text{nth}}|$. Based on this fact, we conclude that the amplitude mode is associated with the nonthermal fixed point, not with the thermal phase transition. This is not expected in the Ginzburg-Landau picture, where the oscillation disappears when the curvature of the free energy potential at the origin changes sign at the thermal critical point.

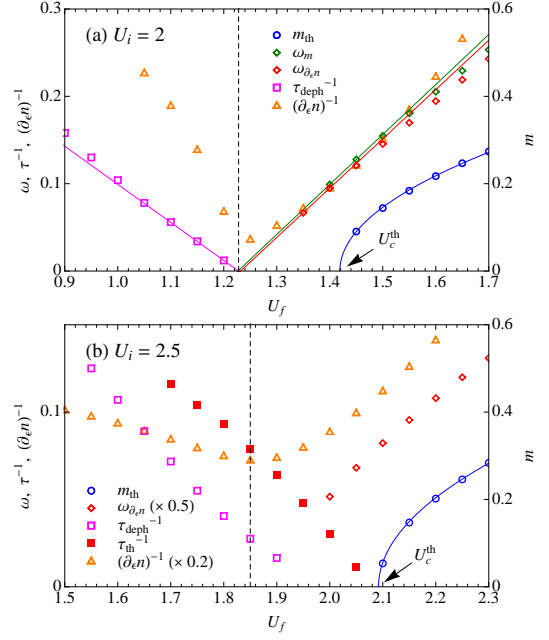


FIG. 4: (color online). Various quantities used to characterize the qualitative change of the behavior around $U_f = U_c^{\text{th}}$ and $U_f = U_*^{\text{nth}}$ (dashed lines) for quenches $U_i \rightarrow U_f$. Solid lines are guides for the eye.

This quasicritical point (or sharp crossover) becomes an exact critical point in the weak-correlation limit, where the dynamics is described by the Hartree approximation. As we show in the Supplemental Material, the Hartree equation is mathematically equivalent to the time-dependent BCS equation, which is known to be integrable with infinitely many conserved quantities [28, 29]. There is a strict transition for the motion of the order parameter from damped oscillation to overdamped decay that is both associated with a diverging dephasing time (overdamped decay) and a vanishing of the amplitude-mode frequency. What we found here is that the qualitative aspects of the transition are maintained even in the regime where the Hartree approximation breaks down ($U \gtrsim 0.5$) due to quantum corrections from higher-order diagrams. In fact, the Hartree equation gives quantitatively very different results in this regime [27].

As one increases U_i , the system spends less time near the nonthermal fixed point, and thermalization occurs earlier. For $U_i = 2.5$ [Fig. 2(b)], coherent amplitude oscillations are not visible anymore, and only a bump structure remains on a short time scale ($t \lesssim 30$) for $U_f > 1.8$. In this interaction regime the system does not show a clear signature of a transition, but a nonthermal crossover behavior is still seen in various quantities [Fig. 4(b)] around $U_f = U_*^{\text{nth}} \sim 1.85$, which is estimated from the maximum of $\partial_\epsilon n$. For $U_f < U_*^{\text{nth}}$, we find that the order parameter m shows a two-step relaxation [Fig. 5(a)]; i.e., the short-time and long-time dynamics have different exponential decay rates. The former is identified to be τ_{deph} , since it is smoothly connected to what we have defined as τ_{deph} in

the previous $U_i = 2$ case. The latter is related to the thermal phase transition where m_{th} disappears, hence denoted by τ_{th} [30]. The obtained τ_{deph} and τ_{th} are shown in Fig. 4(b). Interestingly, in most cases τ_{deph} is larger than τ_{th} , that is, the slow dephasing of m is followed by faster thermalization. Furthermore, thermalization is significantly delayed compared to τ_{th} . At $U_f = 1.9$, for example, $\tau_{\text{th}} = 15.3$ while the delay time of thermalization is > 100 . This allows the order parameter to survive longer than the thermalization time constant.

Finally, let us examine the relaxation around the thermal critical point. Thermalization critically slows down as one approaches the thermal critical point [Fig. 4(b)] with

$$\tau_{\text{th}} \propto |U_f - U_c^{\text{th}}|^{-1}, \quad (1)$$

which, unlike τ_{deph} , remains even when the interaction is increased. Since the critical behavior around the thermal transition is universal, i.e., does not depend on details of the initial state or the the ramp protocol, it can be described by equilibrium properties. In fact, near a thermal (or quantum) critical point the relaxation time is known to behave as $\tau_{\text{th}} \sim |U_f - U_c^{\text{th}}|^{-z\nu}$ [13]. Here ν is the critical exponent that characterizes the divergence of the correlation length, $\xi \sim |U_f - U_c^{\text{th}}|^{-\nu}$, and z is the dynamical critical exponent. Our result (1) is consistent with the mean-field exponents $\nu = \frac{1}{2}$ and $z = 2$ for nonconserved order parameters [13]. Exactly at the thermal critical point ($U_f = U_c^{\text{th}}$), the correlation time diverges, and the order parameter thermalizes in a power law. In Fig. 5(b), we show the log-log plot of m around the thermal critical point ($U_c^{\text{th}} = 2.40$). The curve agrees very well with

$$m \propto t^{-1/2}. \quad (2)$$

This is consistent to the prediction of the dynamical scaling ansatz [13], $m \sim t^{-\beta/z\nu}$, with the mean-field exponent $\beta = \frac{1}{2}$.

We summarize our results in a nonequilibrium phase diagram in Fig. 1(b). The results do not qualitatively change away from half filling [27] or with different initial m or T . In fact, we numerically confirmed with the Hartree equation and the nonequilibrium DMFT that the slightly doped ($\lesssim 5\%$) system can be trapped in a nonthermal ordered state, and that the ‘‘critical’’ behavior at the nonthermal fixed point is the same. Our findings are applicable not only to antiferromagnetic order but also to superconductivity and charge density wave order if one translates the repulsive model to an attractive model [31]. An open question of practical importance is how to access this nonthermal fixed point. While we focused here on interaction quenches, the phenomenon is not specific to the particular quench protocol. For example, we have confirmed that a back-and-forth quench [27] gives similar nonthermal critical behavior with elevated T_{eff} , implying that the overall change of the interaction parameter is not essential. This universality nature of the phenomenon will open up a possible route to experimentally reach the nonthermal fixed point such as heating the system with laser irradiation. Since the order parameter is connected to the energy gap, the nonthermal or-

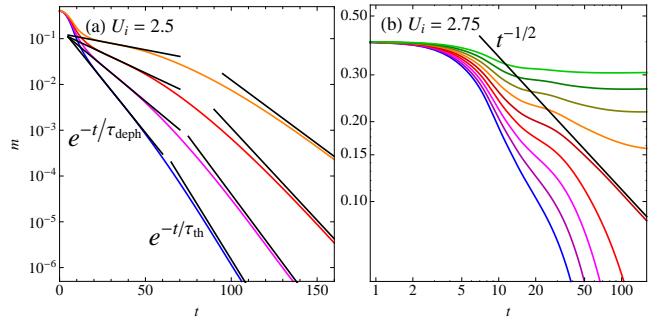


FIG. 5: (color online). (a) The log plot of m for quenches $U_i = 2.5 \rightarrow U_f = 1.6, 1.7, 1.8, 1.9$ from bottom to top. The straight lines show fits of the two exponential relaxations. (b) The log-log plot of m for quenches $U_i = 2.75 \rightarrow U_f = 2.2, 2.25, \dots, 2.6$ from bottom to top. The straight line shows the slope of a power law decay $\propto t^{-1/2}$.

der can be monitored with time-resolved optical and photoemission spectroscopies.

We thank H. Aoki, P. Barmettler, J. Berges, and T. Oka for fruitful discussions. The calculations were carried out on the Brutus cluster at ETH Zurich and on the UniFr cluster. We acknowledge support from the Swiss National Science Foundation (Grant No. PP0022-118866) and FP7/ERC Starting Grant No. 278023.

SUPPLEMENTAL MATERIAL

Hartree approximation

In this section, we derive the Hartree approximation for the antiferromagnetic phase of the Hubbard model, and show that it is mathematically equivalent to the integrable time-dependent BCS equation [28, 29] at arbitrary filling.

Let us define a set of momentum distribution functions using the nonequilibrium (lesser) Green function,

$$n_{k\sigma}^{ab}(t) = (-i)G_{k\sigma}^{ab<}(t, t) \quad (3)$$

$$= N^{-1} \sum_{i \in a, j \in b} e^{i\mathbf{k} \cdot (\mathbf{R}_i - \mathbf{R}_j)} \langle c_{i\sigma}^\dagger(t) c_{j\sigma}(t) \rangle \quad (4)$$

with $a, b = A, B$ sublattice indices and N the number of sublattice sites. The nonequilibrium Green function satisfies the 2×2 Dyson equation

$$\begin{pmatrix} i\vec{\partial}_t + \mu - \Sigma_\sigma^A & -\epsilon_{\mathbf{k}} \\ -\epsilon_{\mathbf{k}} & i\vec{\partial}_t + \mu - \Sigma_\sigma^B \end{pmatrix} * \begin{pmatrix} G_{k\sigma}^{AA} & G_{k\sigma}^{AB} \\ G_{k\sigma}^{BA} & G_{k\sigma}^{BB} \end{pmatrix} = \begin{pmatrix} \delta_c & 0 \\ 0 & \delta_c \end{pmatrix}, \quad (5)$$

and its conjugate equation

$$\begin{pmatrix} G_{k\sigma}^{AA} & G_{k\sigma}^{AB} \\ G_{k\sigma}^{BA} & G_{k\sigma}^{BB} \end{pmatrix} * \begin{pmatrix} -i\overleftarrow{\partial}_{t'} + \mu - \Sigma_{\sigma}^A & -\epsilon_k \\ -\epsilon_k & -i\overleftarrow{\partial}_{t'} + \mu - \Sigma_{\sigma}^B \end{pmatrix} = \begin{pmatrix} \delta_{\mathcal{C}} & 0 \\ 0 & \delta_{\mathcal{C}} \end{pmatrix}, \quad (6)$$

where μ is the chemical potential, Σ_{σ}^a is the local self-energy on sublattice a , $*$ denotes a convolution for time arguments, and $\delta_{\mathcal{C}}$ is the delta function defined on the Keldysh contour \mathcal{C} . In the Hartree approximation, the self-energy is given by

$$\Sigma_{\sigma}^A(t, t') = U(t)n_{\sigma}^A(t)\delta_{\mathcal{C}}(t, t'), \quad (7)$$

$$\Sigma_{\sigma}^B(t, t') = U(t)n_{\sigma}^B(t)\delta_{\mathcal{C}}(t, t'), \quad (8)$$

with $n_{\sigma}^a(t) = \langle c_{i\sigma}^{\dagger}(t)c_{i\sigma}(t) \rangle$ ($i \in a = A, B$ sublattice) the local density. In the presence of AFM order, the local densities are simply

$$n_{\sigma}^A(t) = \bar{n} + \frac{1}{2}\sigma m(t), \quad (9)$$

$$n_{\sigma}^B(t) = \bar{n} - \frac{1}{2}\sigma m(t), \quad (10)$$

where \bar{n} is the average density per site and spin. Using the Dyson equations (5) and (6) with the Hartree approximation, we obtain a closed set of equations of motion for the equal-time lesser Green functions,

$$(i\partial_t + i\partial_{t'})G_{k\sigma}^{AA<}(t, t')|_{t'=t} = \epsilon_k [G_{k\sigma}^{BA<}(t, t) - G_{k\sigma}^{AB<}(t, t)], \quad (11)$$

$$(i\partial_t + i\partial_{t'})G_{k\sigma}^{BB<}(t, t')|_{t'=t} = -\epsilon_k [G_{k\sigma}^{BA<}(t, t) - G_{k\sigma}^{AB<}(t, t)], \quad (12)$$

$$(i\partial_t + i\partial_{t'})G_{k\sigma}^{BA<}(t, t')|_{t'=t} = \epsilon_k [G_{k\sigma}^{AA<}(t, t) - G_{k\sigma}^{BB<}(t, t)] - U(t)m(t)\bar{\sigma}G_{k\sigma}^{BA<}(t, t), \quad (13)$$

$$(i\partial_t + i\partial_{t'})G_{k\sigma}^{AB<}(t, t')|_{t'=t} = -\epsilon_k [G_{k\sigma}^{AA<}(t, t) - G_{k\sigma}^{BB<}(t, t)] + U(t)m(t)\bar{\sigma}G_{k\sigma}^{AB<}(t, t). \quad (14)$$

Equation (3) is used to replace the equal-time Green functions by the corresponding momentum distribution functions, with which the equations read

$$\partial_t [n_{k\sigma}^{AA}(t) + n_{k\sigma}^{BB}(t)] = 0, \quad (15)$$

$$\partial_t [n_{k\sigma}^{BA}(t) + n_{k\sigma}^{AB}(t)] = -iU(t)m(t)\sigma [n_{k\sigma}^{BA}(t) - n_{k\sigma}^{AB}(t)], \quad (16)$$

$$i\partial_t [n_{k\sigma}^{BA}(t) - n_{k\sigma}^{AB}(t)] = 2\epsilon_k [n_{k\sigma}^{AA}(t) - n_{k\sigma}^{BB}(t)] + U(t)m(t)\sigma [n_{k\sigma}^{BA}(t) + n_{k\sigma}^{AB}(t)], \quad (17)$$

$$\partial_t [n_{k\sigma}^{AA}(t) - n_{k\sigma}^{BB}(t)] = -2i\epsilon_k [n_{k\sigma}^{BA}(t) - n_{k\sigma}^{AB}(t)], \quad (18)$$

To make the expression transparent, we adopt a representation analogous to Anderson's pseudospin for the BCS theory [32],

$$f_{\mathbf{k}}^x(t) = \frac{1}{2} \sum_{\sigma} [n_{k\sigma}^{BA}(t) + n_{k\sigma}^{AB}(t)], \quad (19)$$

$$f_{\mathbf{k}}^y(t) = \frac{i}{2} \sum_{\sigma} \sigma [n_{k\sigma}^{BA}(t) - n_{k\sigma}^{AB}(t)], \quad (20)$$

$$f_{\mathbf{k}}^z(t) = \frac{1}{2} \sum_{\sigma} \sigma [n_{k\sigma}^{AA}(t) - n_{k\sigma}^{BB}(t)]. \quad (21)$$

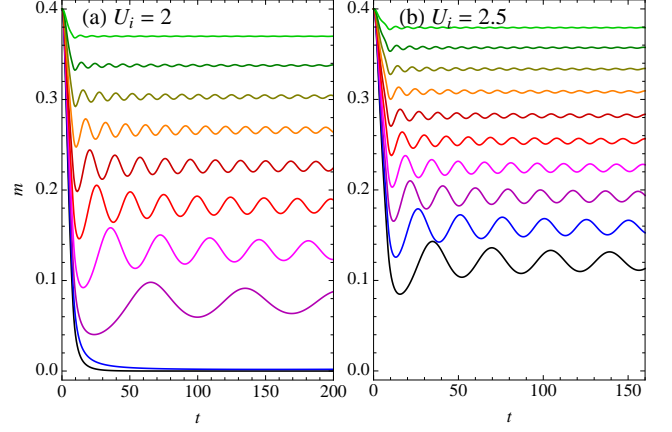


FIG. 6: Time evolution of m calculated with the Hartree approximation for quenches (a) $U_i = 2 \rightarrow U_f = 1.0, 1.1, \dots, 1.9$ (from bottom to top) and (b) $U_i = 2.5 \rightarrow U_f = 1.5, 1.6, \dots, 2.4$ (from bottom to top). The color codes are the same as Fig. 2 in the main text. Note that the temperatures of the initial states are chosen to be different values from those of Fig. 2 in the main text to fix $m(0) = 0.4$.

Then the Hartree equation can be simply written in the form of a ‘Bloch equation’,

$$\partial_t \mathbf{f}_{\mathbf{k}}(t) = \mathbf{b}_{\mathbf{k}}(t) \times \mathbf{f}_{\mathbf{k}}(t), \quad (22)$$

with the pseudospin

$$\mathbf{f}_{\mathbf{k}} = (f_{\mathbf{k}}^x, f_{\mathbf{k}}^y, f_{\mathbf{k}}^z) \quad (23)$$

and an effective magnetic field

$$\mathbf{b}_{\mathbf{k}}(t) = (-2\epsilon_{\mathbf{k}}, 0, U(t)m(t)). \quad (24)$$

The order parameter is self-consistently determined by

$$m(t) = \sum_{\mathbf{k}} f_{\mathbf{k}}^z(t). \quad (25)$$

It turns out that the equation (22) is mathematically equivalent to the time-dependent BCS equation [28, 29] if one appropriately translates the order parameter from the repulsive model to an attractive model [31]. The equation is known to be integrable, and has infinitely many conserved quantities. For example, $n_{k\sigma}^{AA} + n_{k\sigma}^{BB}$ [Eq. (15)] and the ‘length of the pseudospin’

$$|\mathbf{f}_{\mathbf{k}}|^2 \equiv (f_{\mathbf{k}}^x)^2 + (f_{\mathbf{k}}^y)^2 + (f_{\mathbf{k}}^z)^2 \quad (26)$$

are conserved for each \mathbf{k} .

Figure 6 shows the results obtained from the Hartree approximation for the order parameter m . We choose the different temperatures of the initial states from those of Fig. 2 in the main text such that the initial value of the order parameter is the same as in the main text ($m(0) = 0.4$). For $U_i = 2$ [Fig. 6(a)], the overall tendency of the behavior is qualitatively

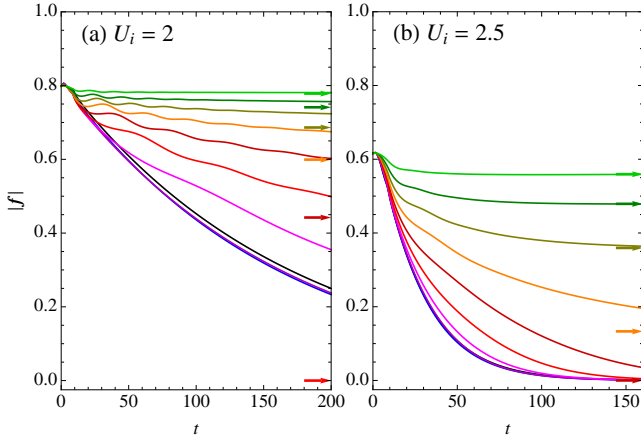


FIG. 7: Time evolution of $|f_k|$ at $\epsilon_k = 0$ calculated with nonequilibrium DMFT for quenches (a) $U_i = 2 \rightarrow U_f = 1.0, 1.1, \dots, 1.9$ (from bottom to top) and (b) $U_i = 2.5 \rightarrow U_f = 1.5, 1.6, \dots, 2.4$ (from bottom to top). The color codes are the same as in Fig. 2 in the main text. The arrows indicate the corresponding thermal values reached in the long-time limit.

similar to what we have observed with the nonequilibrium DMFT calculation in Fig. 2(a) of the main text, apart from the fact that the system never thermalizes within the Hartree calculation, such that the nonthermal transition becomes infinitely sharp. After the quench, m rapidly decreases, and is suddenly trapped in a nonthermal value with coherent oscillation of the amplitude. Between $U_f = 1.1$ and 1.2 , the center of the oscillations gradually approaches zero, and the behavior of m sharply changes from a damped oscillation to an exponential decay at some $U_f = U_*^{\text{nth}}$. However, quantitatively the evolution of m is very different. For example, the center of the oscillations, their frequency, the damping rate, and the transition point (U_*^{nth}) are all different from those of Fig. 2(a) in the main text. This is because the interaction strength that we consider here is already beyond the one ($U < 0.5$) for which the Hartree approximation works. It is thus surprising that the results including higher-order quantum corrections shown in the main text nevertheless share the qualitative features of the Hartree approximation in this interaction regime. For $U_i = 2.5$ [Fig. 6(b)], the qualitative properties remain unchanged within the Hartree approximation, but the sharpness of the transition is lost after quantum corrections are taken into account by nonequilibrium DMFT [Fig. 2(b) in the main text].

To see how the Hartree approximation fails for $U > 0.5$, we plot nonequilibrium DMFT results for $|f_k|$ (26) at $\epsilon_k = 0$ (Fermi energy) in Fig. 7. These quantities would be conserved in the Hartree approximation. At $\epsilon_k = 0$, $|f_k| = |f_k^z|$ since the off-diagonal Green functions ($G_{k\sigma}^{AB}, G_{k\sigma}^{BA}$) are odd functions of ϵ_k . One can calculate $f_k^z|_{\epsilon=0}$ from P_σ^a [Eq. (29) below] using the relation $f_k^z|_{\epsilon=0} = \frac{1}{2} \sum_\sigma (-i)\sigma(P_\sigma^A - P_\sigma^B)$. One can see in Fig. 7(a) that $|f_k|$ is not conserved even for $U_f = 1.0$, but starts to decay immediately after the quench without any plateau. This suggests that the Hartree equation (22) is not

valid on any time scale, except in the very weakly correlated regime ($U < 0.5$). It was already clear from the equilibrium phase diagram [Fig. 1(a)], which shows the Hartree phase boundary as a dashed line, that there are large quantum corrections from higher order diagrams for $U > 0.5$.

Finally, we remark that Eq. (22) holds for “arbitrary filling”, and thus even if the symmetry between the repulsive and attractive models is not valid any more. This suggests that a nonthermal fixed point similar to what we have found at half-filling appears also away from half-filling. In fact, we numerically confirmed with the Hartree equation and the nonequilibrium DMFT that the slightly doped ($\lesssim 5\%$) system can be trapped in a nonthermal ordered state, and that the “critical” behavior at the nonthermal fixed point is the same.

Momentum distribution function

In this section, we show the derivation of the momentum distribution function

$$n_k(t) = \langle c_{k\sigma}^\dagger(t) c_{k\sigma}(t) \rangle, \quad (27)$$

and present the numerical results for the slope of the distribution $\partial_\epsilon n_k$ at $\epsilon_k = 0$ (Fermi energy), which sensitively measures whether and how thermalization takes place.

By definition, one can obtain the momentum distribution (27) from the nonequilibrium Green function (3),

$$n_{k\sigma}(t) = \frac{1}{2} \sum_{ab} (-i) G_{k\sigma}^{ab<}(t, t). \quad (28)$$

The Green function satisfies the 2×2 Dyson equation (5), which can be reduced to a set of 1×1 Dyson equations. To this end, we take the diagonal Green function at $\epsilon_k = 0$, which we denote by

$$P_\sigma^a \equiv G_{k\sigma}^{aa}|_{\epsilon=0} \quad (29)$$

($a = A, B$). It satisfies

$$(i\partial_t + \mu - \Sigma_\sigma^a) * P_\sigma^a = \delta_C. \quad (30)$$

With P_σ^a , the Green functions at arbitrary ϵ_k are given by

$$(i\partial_t + \mu - \Sigma_\sigma^A - \epsilon_k^2 P_\sigma^B) * G_{k\sigma}^{AA} = \delta_C, \quad (31)$$

$$(i\partial_t + \mu - \Sigma_\sigma^B - \epsilon_k^2 P_\sigma^A) * G_{k\sigma}^{BB} = \delta_C, \quad (32)$$

$$G_{k\sigma}^{AB} = \epsilon_k G_{k\sigma}^{AA} * P_\sigma^B, \quad (33)$$

$$G_{k\sigma}^{BA} = \epsilon_k G_{k\sigma}^{BB} * P_\sigma^A. \quad (34)$$

These are equivalent to solving a set of 1×1 Dyson equations.

As is clear from Eqs. (31)-(34), the diagonal Green functions are even functions of ϵ_k , while the off-diagonal Green functions are odd. Thus we have

$$\partial_\epsilon G_{k\sigma}^{AA}|_{\epsilon=0} = \partial_\epsilon G_{k\sigma}^{BB}|_{\epsilon=0} = 0. \quad (35)$$

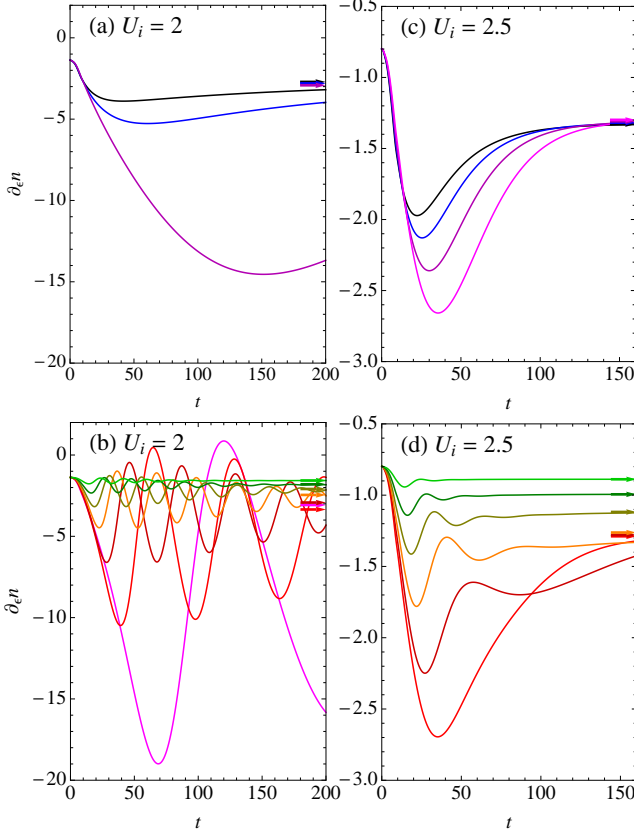


FIG. 8: (Color online). Time evolution of the slope of the momentum distribution $\partial_\epsilon n_k$ at $\epsilon_k = 0$ calculated with nonequilibrium DMFT for quenches $U_i = 2 \rightarrow U_f = 1.0, 1.1, 1.2 (< U_*^{\text{nth}})$ (from top to bottom), (b) $U_i = 2 \rightarrow U_f = 1.3, \dots, 1.9 (> U_*^{\text{nth}})$ (from bottom to top), (c) $U_i = 2.5 \rightarrow U_f = 1.5, 1.6, \dots, 1.8 (< U_*^{\text{nth}})$ (from top to bottom) and (d) $U_i = 2.5 \rightarrow U_f = 1.9, \dots, 2.4 (> U_*^{\text{nth}})$ (from bottom to top). The color codes are the same as Fig. 2 in the main text. The arrows indicate the corresponding thermal values reached in the long-time limit.

To get the first derivative of the off-diagonal Green functions, we take a derivative with respect to ϵ_k and putting $\epsilon_k = 0$ in Eq. (5) to have

$$(i\partial_t + \mu - \Sigma_\sigma^a) * \partial_\epsilon G_{k\sigma}^{ab}|_{\epsilon=0} - G_{k\sigma}^{\bar{a}\bar{b}}|_{\epsilon=0} = 0. \quad (36)$$

From this, we obtain

$$\partial_\epsilon G_{k\sigma}^{AB}|_{\epsilon=0} = P_\sigma^A * P_\sigma^B, \quad (37)$$

$$\partial_\epsilon G_{k\sigma}^{BA}|_{\epsilon=0} = P_\sigma^B * P_\sigma^A. \quad (38)$$

As a result, the slope of the momentum distribution $\partial_\epsilon n_{k\sigma}$ at $\epsilon_k = 0$ is calculated from a convolution,

$$\partial_\epsilon n_{k\sigma}(t)|_{\epsilon=0} = -\frac{i}{2}(P_\sigma^A * P_\sigma^B + P_\sigma^B * P_\sigma^A)^<(t, t). \quad (39)$$

Numerical results for $\partial_\epsilon n$ at $\epsilon_k = 0$ with the same parameters as Fig. 2 in the main text are shown in Fig. 8. For

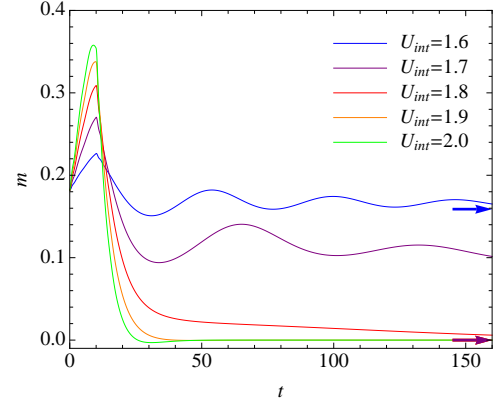


FIG. 9: (Color online). Time evolution of m obtained from the nonequilibrium DMFT for a back-and-forth quench $U = U_i \rightarrow U_{\text{int}} \rightarrow U_i$ with the initial $U_i = 1.5$, $T = 0.056$ and waiting time $t_w = 10$. The arrows indicate the corresponding thermal values reached in the long-time limit.

$U_i = 2.0$ [Fig. 8(a), (b)], there are two clearly different behaviors. When $U_f > 1.2$, $\partial_\epsilon n$ coherently oscillates, which is because a wave mode created in the high energy region of the momentum distribution cascades down to the Fermi energy [Fig. 3(a) in the main text]. The slope $\partial_\epsilon n$ even changes its sign [Fig. 8(b)] if the amplitude of the oscillations is strong enough. This never happens in thermal equilibrium. On longer time scales, the oscillation slowly damps, and the gradient $\partial_\epsilon n$ finally converges to the corresponding thermal value (thermalization). A sharp change occurs between $U_f = 1.2$ and 1.3 , where the amplitude of the oscillation in $\partial_\epsilon n$ is greatly enhanced, and even appears to diverge $\propto |U_f - U_*^{\text{nth}}|^{-1}$ with $U_*^{\text{nth}} = 1.23$ [see the plot of the inverse of the steepest slope $(\partial_\epsilon n)^{-1} \equiv (\max_t \{|\partial_\epsilon n(t)|\})^{-1}$ in Fig. 4(a) of the main text]. As a result, a sharp jump of the momentum distribution starts to appear at the Fermi energy [Fig. 3(a) in the main text]. For $U_f \leq 1.2$, $\partial_\epsilon n$ overdamps without any oscillation. This qualitative change of the behavior of $\partial_\epsilon n$ occurs at the same point ($U_f = U_*^{\text{nth}}$) as that of the order parameter m discussed in the main text. For $U_i = 2.5$ [Fig. 8(c), (d)], the enhancement of $\partial_\epsilon n$ is suppressed due to the limited life-time of the trapped state. However, one can still see a crossover of the relaxation behavior of n_k from damped oscillation to overdamped decay around $U_f \sim 1.85$, the value of U_f for which the “steepest Fermi surface” is reached during the time evolution. Thus we use the steepest n_k as a measure of the nonthermal transition point (U_*^{nth}) in the main text.

Quench protocol dependence

In this section, we discuss how the nonthermal quasi-stationary ordered state that has been found in the main text depends on the interaction quench protocol. In the main text, we concentrated on the linear change of the interaction,

$U(t) = U_i + (U_f - U_i)t/t_q$ ($0 \leq t \leq t_q$) with $t_q = 8$ fixed, to go across the phase transition boundary. However, it should be noted that the phenomenon is not specific to this quench protocol, but is rather general. For example, a qualitatively similar nonthermal state is found for a wide range of t_q . In particular, we numerically confirmed that a sudden quench (i.e., $t_q = 0$) can lead to a nonthermal trapped state, although in this case the excitation energy is relatively large so that the nonthermal AFM region in Fig. 1(b) of the main text shrinks.

As a further example, we consider a back-and-forth quench protocol, in which the interaction changes step-wise as $U(t) = U_i$ ($t < 0$), $= U_{int}$ ($0 < t < t_w$), and $= U_i$ ($t > t_w$) with t_w the waiting time (see inset in Fig. 9). This back-and-forth quench is a computationally convenient way of injecting energy into the system. In Fig. 9, we show the time evolution of m for $U_i = 1.5$ and various U_{int} and $t_w = 10$. As one can see, the relaxation behavior qualitatively changes from a damped oscillation to an exponential decay as U_{int} is varied. The magnetization m oscillates around a nonzero, nonthermal value for a long time even in cases where the thermalized value is zero ($U_{int} = 1.7$ in Fig. 9). This protocol corresponds to an effective heating without an overall change of the interaction between the initial and final states. Thus, the trapping phenomenon is not specific to a particular interaction quench, but can be induced by an external perturbation that increases the effective temperature of the system, which suggests various possible and realistic ways of reaching a state controlled by the nonthermal fixed point, such as laser excitations.

[1] T. W. B. Kibble, *J. Phys. A* **9**, 1387 (1976).
 [2] W. H. Zurek, *Nature (London)* **317**, 505 (1985).
 [3] F. Schmitt, P. S. Kirchmann, U. Bovensiepen, R. G. Moore, L. Rettig, M. Krenz, J.-H. Chu, N. Ru, L. Perfetti, D. H. Lu, et al., *Science* **321**, 1649 (2008).
 [4] R. Yusupov, T. Mertelj, V. V. Kabanov, S. Brazovskii, P. Kusar, J.-H. Chu, I. R. Fisher, and D. Mihailovic, *Nat. Phys.* **6**, 681 (2010).
 [5] D. Fausti, R. I. Tobey, N. Dean, S. Kaiser, A. Dienst, M. C. Hoffmann, S. Pyon, T. Takayama, H. Takagi, and A. Cavalleri, *Science* **331**, 189 (2011).
 [6] A. L. Cavalieri, N. Muller, T. Uphues, V. S. Yakovlev, A. Baltuska, B. Horvath, B. Schmidt, L. Blumel, R. Holzwarth, S. Hendel, et al., *Nature (London)* **449**, 1029 (2007).

[7] I. Bloch, J. Dalibard, and W. Zwerger, *Rev. Mod. Phys.* **80**, 885 (2008).
 [8] J. Berges, S. Borsányi, and C. Wetterich, *Phys. Rev. Lett.* **93**, 142002 (2004).
 [9] M. Moeckel and S. Kehrein, *Phys. Rev. Lett.* **100**, 175702 (2008).
 [10] M. Eckstein, M. Kollar, and P. Werner, *Phys. Rev. Lett.* **103**, 056403 (2009).
 [11] M. Kollar, F. A. Wolf, and M. Eckstein, *Phys. Rev. B* **84**, 054304 (2011).
 [12] J. Berges, A. Rothkopf, and J. Schmidt, *Phys. Rev. Lett.* **101**, 041603 (2008).
 [13] P. C. Hohenberg and B. I. Halperin, *Rev. Mod. Phys.* **49**, 435 (1977).
 [14] A. Polkovnikov, K. Sengupta, A. Silva, and M. Vengalattore, *Rev. Mod. Phys.* **83**, 863 (2011).
 [15] D. E. Feldman, *Phys. Rev. Lett.* **95**, 177201 (2005).
 [16] A. Mitra, S. Takei, Y. B. Kim, and A. J. Millis, *Phys. Rev. Lett.* **97**, 236808 (2006).
 [17] C. Kollath, A. M. Läuchli, and E. Altman, *Phys. Rev. Lett.* **98**, 180601 (2007).
 [18] P. Barmettler, M. Punk, V. Gritsev, E. Demler, and E. Altman, *Phys. Rev. Lett.* **102**, 130603 (2009).
 [19] A. Koga and P. Werner, *Phys. Rev. A* **84**, 023638 (2011).
 [20] P. Werner, N. Tsuji, and M. Eckstein, *Phys. Rev. B* **86**, 205101 (2012).
 [21] N. Tsuji, T. Oka, P. Werner, and H. Aoki, *Phys. Rev. Lett.* **106**, 236401 (2011).
 [22] N. Tsuji, T. Oka, H. Aoki, and P. Werner, *Phys. Rev. B* **85**, 155124 (2012).
 [23] A. Georges, G. Kotliar, W. Krauth, and M. J. Rozenberg, *Rev. Mod. Phys.* **68**, 13 (1996).
 [24] J. K. Freericks, V. M. Turkowski, and V. Zlatić, *Phys. Rev. Lett.* **97**, 266408 (2006).
 [25] W. Metzner and D. Vollhardt, *Phys. Rev. Lett.* **62**, 324 (1989).
 [26] F. Werner, O. Parcollet, A. Georges, and S. R. Hassan, *Phys. Rev. Lett.* **95**, 056401 (2005).
 [27] See Supplemental Material for the Hartree approximation, the momentum distribution function, and the quench protocol dependence.
 [28] R. A. Barankov and L. S. Levitov, *Phys. Rev. Lett.* **96**, 230403 (2006).
 [29] E. A. Yuzbashyan and M. Dzero, *Phys. Rev. Lett.* **96**, 230404 (2006).
 [30] In the previous case ($U_i = 2$), the crossover from dephasing to thermalization could not be observed, because it occurs at times which cannot be reached in our simulation.
 [31] H. Shiba, *Prog. Theor. Phys.* **48**, 2171 (1972).
 [32] P. W. Anderson, *Phys. Rev.* **112**, 1900 (1958).